Charge-to-Spin Interconversion in Low-Symmetry Topological Materials

Marc Vila,[*,†,‡] Chuang-Han Hsu,[¶,§] Jose H. Garcia,[†] L. Antonio Benítez,[†,‡] Xavier Waintal,[‖] Sergio O. Valenzuela,[†,⊥] Vitor M. Pereira,[§] and Stephan Roche[*,†,⊥]

†*Catalan Institute of Nanoscience and Nanotechnology (ICN2), CSIC and BIST, Campus UAB, Bellaterra, 08193 Barcelona, Spain*

‡*Department of Physics, Universitat Autònoma de Barcelona, Campus UAB, Bellaterra, 08193 Barcelona, Spain*

¶*Department of Electrical and Computer Engineering, National University of Singapore, Singapore 117576, Singapore*

§*Centre for Advanced 2D Materials and Graphene Research Centre, National University of Singapore, Singapore 117546, Singapore*

‖*Univ. Grenoble Alpes, CEA, IRIG-PHELIQS, 38000 Grenoble, France*

⊥*ICREA–Institució Catalana de Recerca i Estudis Avançats, 08010 Barcelona, Spain*

E-mail: marc.vila@icn2.cat; stephan.roche@icn2.cat

In this supplemental material, we explain in detail the derivation and fitting of the tight-binding model to density functional theory calculations; the role of the spin Berry curvature in the spin Hall conductivity of $MoTe_2$; the implementation of such model in

Landauer-Büttiker calculations to extract the spin diffusion length and the spin Hall angle; the implementation of the model in Kubo-Bastin calculations to also extract the spin Hall angle; the relation between the (persistent) spin textures and the spin diffusion lengths; extra results showing the spin relaxation of in-gap states and the comparison between $1T_d$-$MoTe_2$ and $1T'$-$MoTe_2$; and the use of the Bloch spin diffusion equations to measure the canted spin Hall effect in a nonlocal transport experiment.

Ab-initio calculations and tight-binding model

Density functional theory (DFT) calculations of transition metal dichalcogenide (TMD) monolayers $1T_d$-$MoTe_2$ and $1T_d$-WTe_2 were performed using the VASP package.[1–3] Details of the simulations can be found in previous works.[4–6] From the DFT calculations, a tight-binding model was interpolated in the Wannier basis via Wannier90[7] and applied for calculating the spin texture.

To construct our 4-band real space tight binding model, we begin by elaborating a 4-band $k \cdot p$ model based on the symmetries of $1T'$ and $1T_d$ TMDs. Both phases present a mirror symmetry operation in the yz plane (M_x) but only $1T'$ has inversion symmetry $\mathcal{I}$. We consider the point group symmetry C_{2h} of the $1T'$ phase and additional terms are added to reduce it to the $1T_d$ phase. The irreducible representations (irreps) of some states at Γ in $1T_d$-$MoTe_2$ are shown in Fig. 1c. For the C_{2h} point group, we choose two irreducible representations for the $p_y\,(B_u)$ valence band and $d_{yz}\,(A_g)$ conduction band.[8] This allows

Table 1: Character table for the point group C_{2h}.

	C_{2x}	i	$\sigma_h\,(M_x)$
A_g	+1	+1	+1
B_u	-1	-1	+1
A_u	+1	-1	-1
B_g	-1	+1	-1

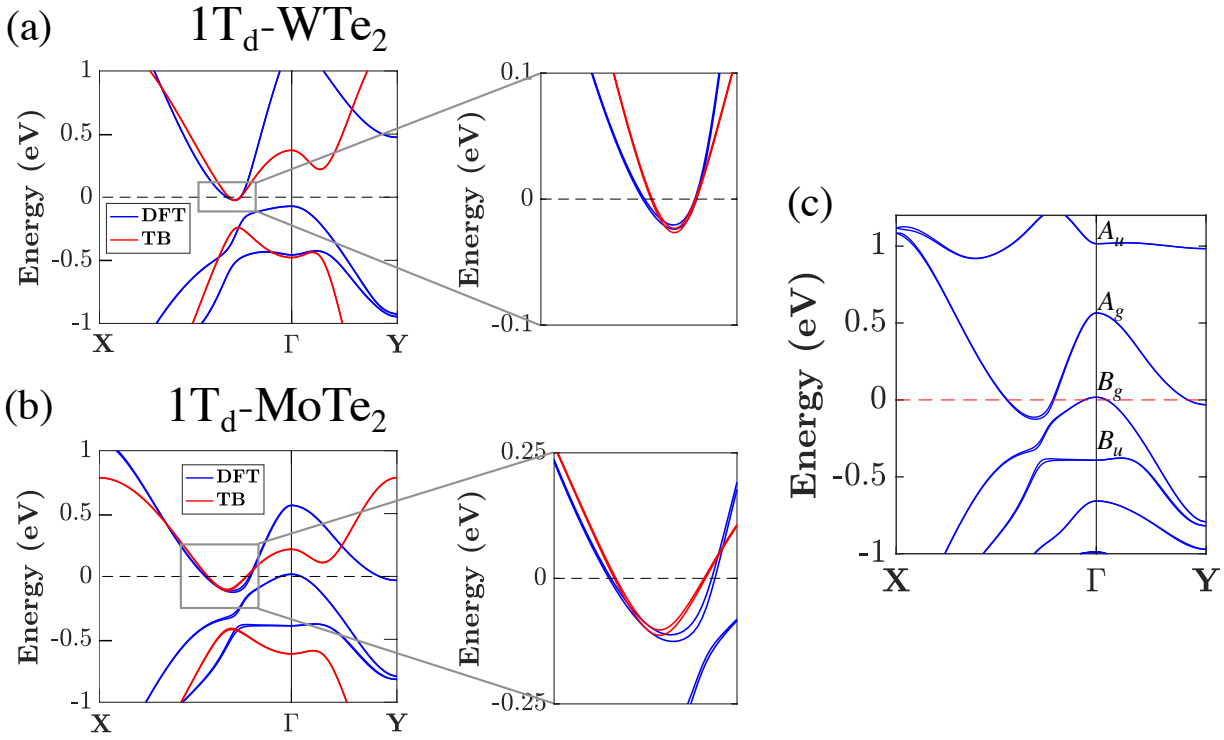

Figure 1: (a) Comparison of band structure of monolayer $1T_d$-WTe_2 obtained from DFT (blue) and 4-bands tight-binding model (red). (b) Same as in (a) but for $1T_d$-$MoTe_2$. (c) DFT band structure of monolayer $1T_d$-$MoTe_2$ and the irreducible representation of states near Γ.

us to assign τ_z as the inversion operator (I) for this basis. The parabolic conduction and valence bands can be expressed as $m_p k^2 \tau_0 + (m_d k^2 + \delta)\,\tau_z$, where $m_p - m_d$ and $m_p + m_d$ are effective masses of p_y and d_{yz}, and δ is the strength of band inversion at Γ. Away from Γ, any generic k points have the time-reversal $\mathcal{T} = i\sigma_y K$ symmetry, where $\mathcal{T}^2 = -1$ for a spinor. Note that we adopt τ_α and σ_α Pauli matrices for the orbital and spin degrees of freedom, with $\alpha = x, y, z$. At $k_x = 0$, states have the mirror symmetry $M_x = i\sigma_x \otimes \tau_0$; at $k_y = 0$, states have the rotational symmetry $C_{2x} = IM_x = i\sigma_x \otimes \tau_z$. By considering these symmetries, the Hamiltonian with additional symmetry-allowed terms up to first order in k reads,

$$\begin{aligned} H_{kp}(k_x, k_y) &= m_p k^2 \tau_0 + \left(m_d k^2 + \delta\right) \tau_z + \beta k_y \sigma_0 \otimes \tau_y \\ &\quad + \Lambda_x k_y \sigma_x \otimes \tau_x + \Lambda_y k_x \sigma_y \otimes \tau_x + \Lambda_z k_x \sigma_z \otimes \tau_x \\ &\quad + \eta \sigma_0 \otimes \tau_x, \end{aligned} \tag{1}$$

where the third term $\propto \beta$ in the first line gives the crystalline anisotropy between x and y. Terms Λ_α in the second line are the spin-orbit coupling (SOC) for spin-α, and the last term breaks the inversion symmetry, describing in this way either $1\mathrm{T}'$ ($\eta = 0$) or $1\mathrm{T}_\mathrm{d}$ ($\eta \neq 0$).

To map H_{kp} into a rectangular lattice, the k vectors are restored back to periodic functions via the expansions $\sin(k) \approx k + O(k^3)$ and $\cos(k) \approx 1 - k^2/2 + O(k^4)$. Using $\sin(k) = \left(e^{ik} - e^{-ik}\right)/2i$ and $\cos(k) = \left(e^{ik} + e^{-ik}\right)/2$, the tight-binding model can be written down according to the phase $Ce^{i\boldsymbol{k}\cdot\boldsymbol{a}}$, where $\boldsymbol{a} = a_x\hat{\boldsymbol{x}} + a_y\hat{\boldsymbol{y}}$ is the nearest hopping vector which also

equates to the lattice constant in this case:

$$\begin{aligned} H_k(k_x,k_y) &= m_p\left[4-2\cos\left(k_xa_x\right)-2\cos\left(k_ya_y\right)\right]\tau_0+\left(m_d\left[4-2\cos\left(k_xa_x\right)-2\cos\left(k_ya_y\right)\right]+\delta\right)\tau_z \\ &+\Lambda_x\sin\left(k_ya_y\right)\sigma_x\otimes\tau_x+\Lambda_y\sin\left(k_xa_x\right)\sigma_y\otimes\tau_x+\Lambda_z\sin\left(k_xa_x\right)\sigma_z\otimes\tau_x \\ &+\beta\sin\left(k_ya_y\right)\sigma_0\otimes\tau_y+\eta\sigma_0\otimes\tau_x \end{aligned} \tag{2}$$

In the second quantization representation, H_k becomes

$$\begin{aligned} H=&\sum_{i,s}(\Delta+4m_d+\delta)c_{i,s}^{\dagger}c_{i,s}-\sum_{\langle ij\rangle,s}(m_p+m_d)c_{i,s}^{\dagger}c_{j,s} \\ &+\sum_{i,s}(\Delta-4m_d-\delta)d_{i,s}^{\dagger}d_{i,s}-\sum_{\langle ij\rangle,s}(m_p-m_d)d_{i,s}^{\dagger}d_{j,s} \\ &-\sum_{\langle ij\rangle,s}\frac{\beta}{2}(\hat{\boldsymbol{l}}_{ij}\cdot\hat{\boldsymbol{y}})\,c_{i,s}^{\dagger}d_{j,s}+\sum_{i,s}\eta c_{i,s}^{\dagger}d_{i,s} \\ &-\sum_{\langle ij\rangle}\sum_{ss'}\frac{i}{2}(\boldsymbol{\Lambda}_{ss'}\times\hat{\boldsymbol{l}}_{ij})\cdot(\hat{\boldsymbol{y}}+\hat{\boldsymbol{z}})c_{i,s}^{\dagger}d_{j,s'}. \end{aligned} \tag{3}$$

Here, $c_{i,s}^{\dagger}(c_{i,s})$ and $d_{i,s}^{\dagger}(d_{i,s})$ are the creation (annihilation) operators of an electron in the p_z and d_{yz} orbitals at the i-th position with spin s. The symbol $\langle i,j\rangle$ denotes the summation over the nearest-neighbors of site i, with $\hat{\boldsymbol{l}}_{ij}$ being a unit vector connecting the site i with its nearest neighbor in j and $\hat{\boldsymbol{y}}$ ($\hat{\boldsymbol{z}}$) is a unit vector pointing to the y (z) direction. The spin-orbit coupling terms are included in $\boldsymbol{\Lambda}_{ss'}=(\Lambda_x\sigma_x,-\Lambda_y\sigma_y,\Lambda_z\sigma_z)$. Finally, Δ is a constant energy shift (also absorbing the factor $4m_p$ from Eq. (2)) to match the Fermi level from the DFT results.

Next, we fit Eq. (2) to the DFT calculations. This fit includes not only the band dispersion, but the spin splitting and importantly, the spin texture. The bands and spin splitting comparison for $1T_d$-WTe_2 can be seen in Fig. 1a. Because the main goal is to carry out large-scale simulations of realistic geometries, the size of our model needs to be

small, and as a consequence, the agreement between the tight-binding and DFT is not perfect throughout the Brillouin zone. However, we favor the fit to the energies relevant for transport, that is, in the vicinity of the Fermi level at the bottom of the conduction band. In this energy window, both the band dispersion and spin splitting are correctly reproduced, as shown in the zommed-in view of Fig. 1a. We note that our model does not capture the topmost valence band, but rather the second topmost band. However, such topmost valence band (with irreducible representation B_g) is not important to reproduce the band inversion and nontrivial topology, as we need bands with opposite parity at Γ to that end[9] (see Fig. 1c). Thus, as long as we restrict ourselves to energies in the conduction band near the Fermi level, our 4-band model is sufficient. Furthermore, we show in Fig. 1b the comparison between our model and the DFT bands of $1T_d$-$MoTe_2$. In this case, the topmost valence band does cross the Fermi level near Γ in addition to the appearance of a small electron pocket at the Y point also crossing the Fermi level. Nevertheless, the hole pocket at Γ and the electron pocket at Y present a very small Fermi surface and thus it is expected that the conduction band states along the $\Gamma - X$ path dominate in transport properties. In this work, we chose to focus on $MoTe_2$ given the recent experimental findings concerning the canted spin Hall effect in this material,[5,10] but similar qualitatively results can be expected for WTe_2 given that our model applies to both compounds. We note that the Fermi level crossing of the topmost valence band shown in the DFT results does not invalidate the results originating from our 4-band model since the absence or presence of a band gap in $1T_d$-$MoTe_2$ monolayers is still a controversial issue both in DFT calculations (results are very sensitive to the functional and lattice parameters)[8,11–13] and in experiments,[14–18] and even if the gap is closed, it can be opened using strain engineering.[19]

The values of the parameters of the tight binding are also chosen so as to fit the spin texture. The spin texture for spin α at a given energy E is calculated as $\langle k|\sigma_\alpha f(\epsilon(k)-E)|k\rangle$, where $f(\epsilon(k)-E)$ is a broadening function centered at E, in this case chosen to be a derivative

of the Fermi-Dirac distribution at temperature $T = 300$ K. To corroborate the validity of our model, we show the spin texture calculated with the 4-band model and DFT for two distinct energies: at the Fermi level and near the bottom of the conduction band ($E = -100$ meV). The results are shown in Figs. 2 and 3, where we present the spin texture for the two conduction bands of $MoTe_2$. For all cases, our tight-binding correctly reproduces the DFT features, namely, a spin texture pointing mainly along y and z with opposite signs for each of the bands. The values of the fitted parameters for $1T_d$-$MoTe_2$ are listed in Table 2.

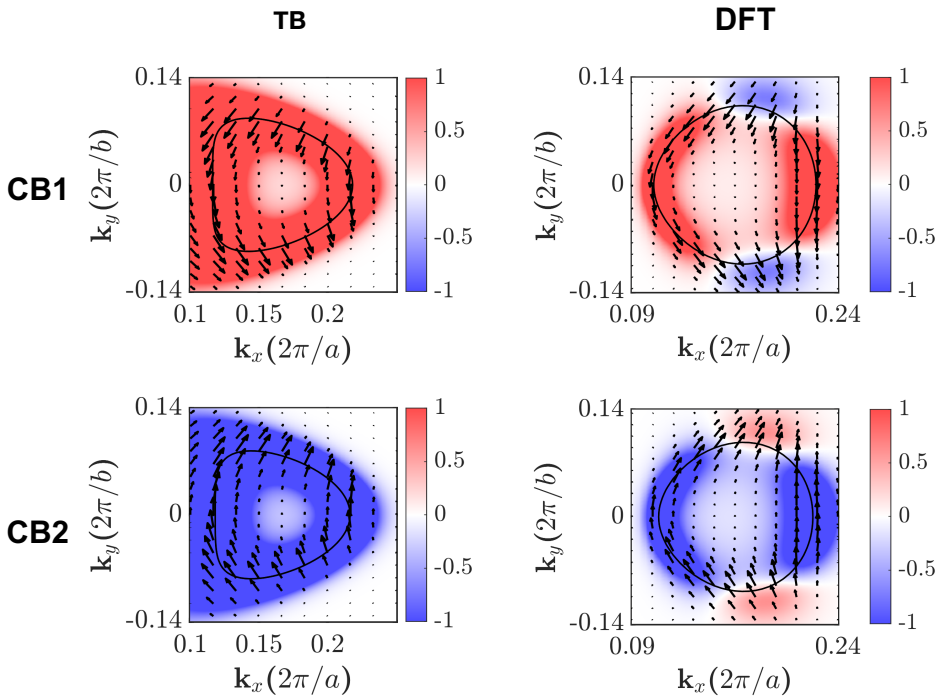

Figure 2: Spin texture of $1T_d$-$MoTe_2$ monolayer at the Fermi level ($E = 0$) computed with the tight-binding model (left) and DFT (right) for the two conduction bands (CB1, CB2).

Table 2: DFT-fitted parameters for the $1T_d$-$MoTe_2$ 4-band tight-binding model (units in meV).

m_p	m_d	δ	β	η	Λ_x	Λ_y	Λ_z	Δ
-67.1	-417.0	415.3	432.3	5.4	94.8	159.2	-89.6	-467.8

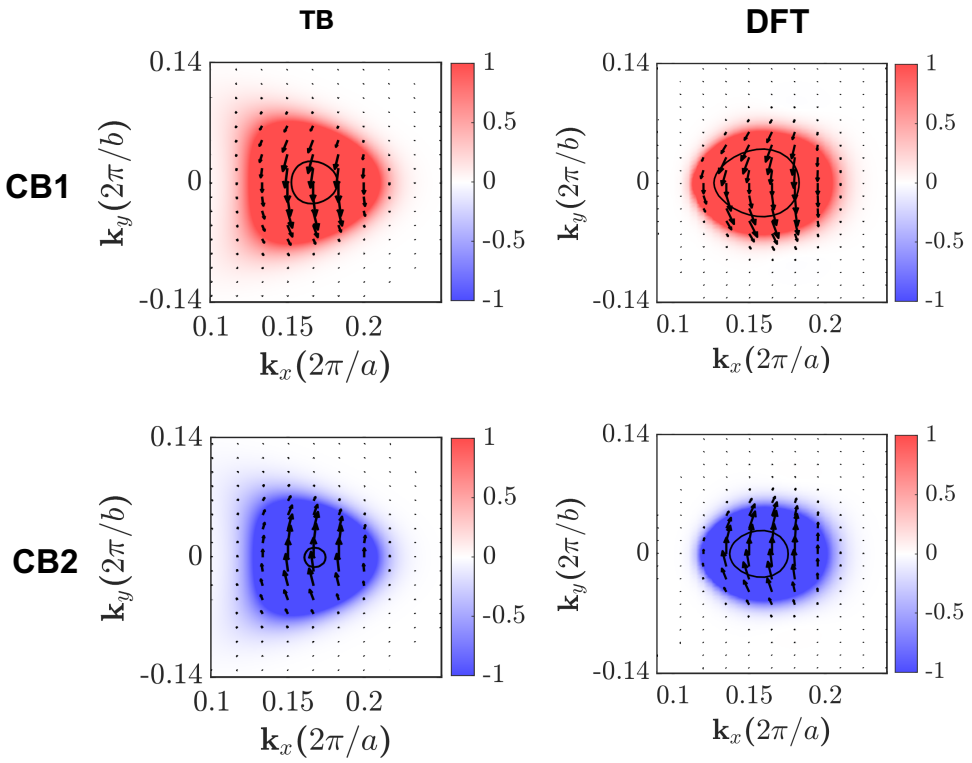

Figure 3: Spin texture of $1T_d$-$MoTe_2$ monolayer at $E = -100$ meV computed with the tight-binding model (left) and DFT (right) for the two conduction bands (CB1, CB2).

Remarks on the spin Berry curvature

The monolayer nature of TMDs and their nontrivial band topology are both important ingredients for the existence of a large and unconventional spin Hall effect (SHE). Specific symmetry reductions with respect to that of the 3D bulk form of these crystals are essential conditions for the existence of non-zero elements of the spin Hall conductivity (SHC) tensor, σ_{ij}^{α}, beyond the conventional one, i.e. σ_{xy}^{z} and its cyclic permutations; such symmetry reduction is ensured in the monolayers we consider. This constraint is explicitly illustrated in Fig. 5 of reference[5] which compares the SHC calculated for a 3D bulk crystal and for a 5-layer slab.

In this sense, having a mono- or few-layer slab is a *necessary condition* to observe the anomalous SHC components irrespective of the underlying nontrivial band topology (in contrast to the conventional component σ_{xy}^{z} which is finite in the 3D bulk as well). But it is *not a sufficient condition* because the magnitude of the SHC, when allowed, is determined by the so-called spin Berry curvature (SBC). The essential topological aspect here arises from the band inversion that occurs at the Γ point, as illustrated in the schematic of Fig. 4.

While the spin-orbit coupling lifts the degeneracy at the Q points where the inverted pair of bands intersect, the regions near Q retain locally large spin Berry curvatures (SBCs). The SBC associated with band n corresponds to the quantity:

$$\Omega_{n,ij}^{\alpha}(\boldsymbol{k}) = -2\mathrm{Im}\sum_{n'\neq n}\frac{\langle n\boldsymbol{k}|\hat{J}_{i}^{\alpha}|n'\boldsymbol{k}\rangle\langle n\boldsymbol{k}|\hat{v}_{j}|n'\boldsymbol{k}\rangle}{(E_{n\boldsymbol{k}}-E_{n'\boldsymbol{k}})^{2}}, \tag{4}$$

where $\hat{J}_{i}^{\alpha}$ represents the i-th component of the spin current operator with spins polarized along α, $\hat{v}_{j}$ is j-th component of the velocity operator and $E_{n\boldsymbol{k}}$ is the energy of the state $|n\boldsymbol{k}\rangle$. The SBC gives the k- and band-projected SHC up to a constant prefactor:

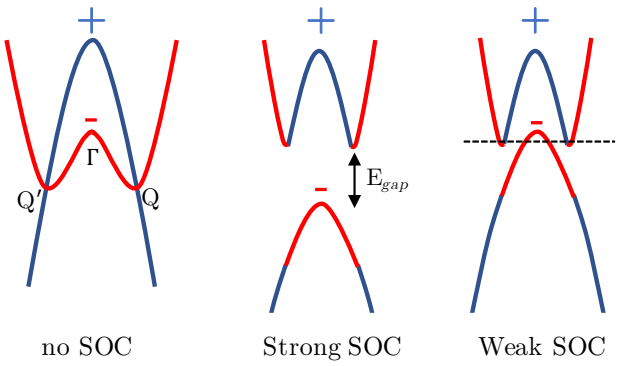

Figure 4: Illustration of the band inversion at the Γ point and the emergence of the electron pockets at Q and Q′ as a result of degeneracy lifting by SOC. The symbols "+" and "-" refer to the parity eigenvalues at Γ. See Fig. 1 for the actual DFT bandstructure of $MoTe_2$ and WTe_2.

$$\sigma_{ij}^{\alpha} = e\hbar \int_{BZ} \frac{d\boldsymbol{k}}{(2\pi)^3} \sum_n f_{n\boldsymbol{k}} \Omega_{n,ij}^{k}(\boldsymbol{k}), \tag{5}$$

with e being the electron's charge and $f_{n\boldsymbol{k}}$ the electron distribution function. In Fig. 5 below, we show a k-resolved map of the quantity under the integral of Eq. 5, that is

$$\sum_n f_{n\boldsymbol{k}} \Omega_{n,ij}^{k}(\boldsymbol{k}), \tag{6}$$

generated with Eq. (2) and with the same parameters used for Fig. 1 in the main manuscript. For definiteness, we look here specifically at the case relevant for the anomalous component σ_{xy}^{y} of the SHC. Each panel of Fig. 5 shows the k-resolved SBC in the vicinity of the Q point in the Brillouin zone, at two representative values of Fermi energy: the ground-state E_F we obtain in DFT and very near the bottom of the two conduction bands ($E = -100$ meV). The important observation to make is that, as conveyed by the color scale, the magnitude of the SBC increases when E approaches the bottom of the conduction pockets (the magnitude is higher in the right plot). This is even better illustrated in Fig. 6, where we show the same

quantity, but as a function of energy along a cut with $k_y = 0$. It can be clearly seen that the magnitude of the SBC is maximal at the bottom of the conduction pockets and decreases relatively quickly to zero when we increase the energy. We refer to this behavior as SBC *hotspots* associated with the band minima.

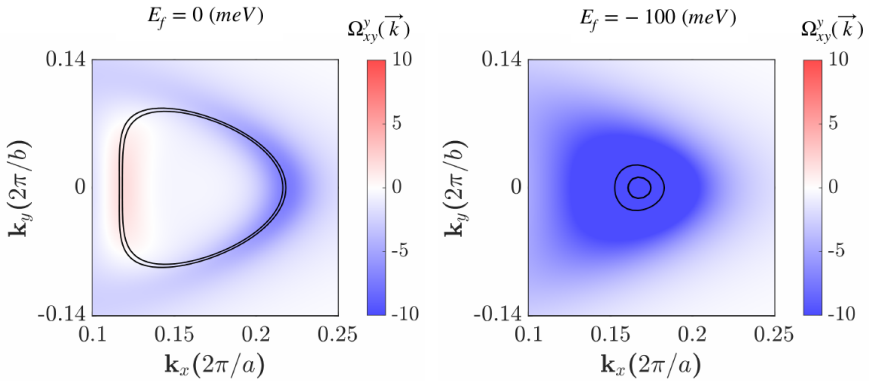

Figure 5: Momentum-resolved spin Berry curvature, defined in Eq. (6) above, near the Q point in the Brillouin zone, at two representative values of Fermi energy: the ground-state E_F (left) and very near the bottom of the two conduction bands, $E = -100$ meV (right).

Now, the existence and qualitative behavior of this SBC is itself a byproduct of the underlying band inversion at the Γ point that is also responsible for the nontrivial band topology. This is because the opposite parity of the inverted bands (cf. Fig. 4) makes these monolayers either fully or close into the 2D topological insulator state (quantum spin Hall insulator, or QSHI), as first predicted by Qian et al.[8] and recently confirmed experimentally in the case of WTe_2.[20–24] Whether a robust QSHI state is realized or not depends on the magnitude of the SOC, specifically whether the SOC is strong enough to open a full gap, as illustrated in the central panel of Fig. 4. As in this manuscript we consider the situation where E_F lies in the conduction band, the quantum spin Hall state is not itself under consideration and is, in fact, immaterial for our results and conclusions, which reflect the behavior expected in either of the two cases labeled "weak" and "strong" SOC in Fig. 4. Nevertheless, the influence of the underlying band inversion and the lifting of degeneracy at the band-crossing

points caused by the SOC is, of course, present and influences the character of the Bloch eigenstates over a significant range of energies around the avoided band crossing. Since the electron pockets at Q are a direct result of this degeneracy lifting, and since E_F is naturally placed in this range of energies, the spintronic response of this system can take maximal advantage of the local hotspots of SBC that we see near the Q pockets in Fig. 6. A brief way to state this on more general grounds is this: in the absence of SOC, we would have E_F slightly above Dirac cones located at the Q points; the Dirac cones acquire a finite mass/gap as a result of the finite SOC; concomitantly, a finite (spin) Berry curvature appears which is maximal near the Dirac gap.

We can, in fact, see a direct and practical manifestation of this in the inset of Fig. 3 of the manuscript, which shows the energy dependence of the spin Hall angle (directly proportional to the SHC, and hence to the SBC): the spin Hall angle increases monotonically as E moves towards the bottom of the conduction band. Consequently, if we note that the band inversion and its associated nontrivial topology is an "accidental" feature of this class of systems - not dictated by crystalline symmetry but by the particular magnitude of physical parameters -, we reach the conclusion that symmetry conditions (in particular those specific to mono- or few-layer slabs) and nontrivial topology are equally important: while the first is necessary, the existence and robustness of the second determines the large magnitudes and energy dependence observed for σ^y_{xy}.

Landauer-Büttiker simulations

Two-terminal calculations

To study spin transport in a experimentally relevant regime, we perform Landauer-Büttiker calculations in a system where the charge and spin transport is diffusive. To do so, we add

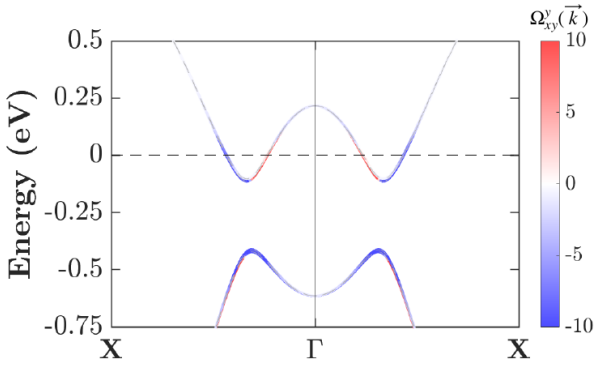

Figure 6: Superimposing the total spin Berry curvature (see Eq. (6) above; color scale) onto the TB-effective band dispersion. It progressively diminishes when moving away from the local extrema at the Q points.

Anderson disorder to the Hamiltonian in Eq. (3) to model inhomogeneities in real samples

$$H_A = \sum_i U_i c^\dagger_{i,s} c_{i,s} + \sum_i U_i d^\dagger_{i,s} d_{i,s}, \tag{7}$$

where U_i is a potential added at each position i with values randomly chosen from a uniform distribution with range $U_i \in [-U/2, U/2]$. We note that both orbitals present the same U_i for a given i, that is, this disorder is diagonal in both spin and orbital space.

The effect of the Anderson disorder is to produce elastic scattering giving rise to a finite mean free path l_e. The first step toward performing realistic spin transport simulations is to obtain l_e, so that our system sizes can be larger than l_e. To that end, we use the Kwant package[25] to implement the real-space tight-binding (Eq. (3)) on a rectangular lattice and calculate the two-terminal conductance (G_{2T}). We use the DFT values $a_x = 3.4607$ Å and $a_y = 6.3066$ Å for the lattice parameters, where a_x and a_y are the lattice constants along the x and y direction, respectively. Unless stated otherwise, we chose the x axis as the semi-infinte transport direction. Therefore, our system (also denoted device or scattering region hereafter) has a finite width w and length L as indicated in Fig. 7. We attach two semiinfinite leads at $x = 0$ and $x = L$, and model them with the same real-space tight-

binding, but without Anderson disorder. To extract the mean free path, we need to calculate how G_{2T} decays with length, and fit the diffusive part of the decay to[26]

$$G_{2T} = \frac{e^2}{h}\frac{Ml_e}{x}. \tag{8}$$

Here, M is the number of modes or subbands present at energy E due to the finite size along the y direction. We note that this equation is equivalent to $G_{2T} = \frac{\sigma w}{x}$, where σ is the electrical conductivity. These equations are only valid when transport is diffusive, but in a quasi-1-dimensional (1D) system achieving diffusive regime may be complicated as the transport may change quickly from ballistic to localized. Nevertheless, an easy way to visualize that is by plotting the electrical conductivity $\sigma = \frac{G_{2T}x}{w}$ versus channel length and observe when its magnitude remains constant (see Fig. 8).

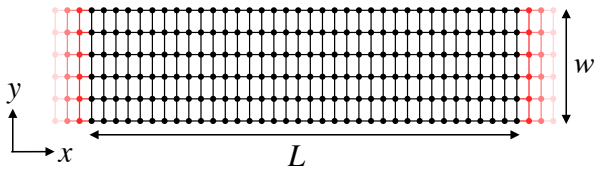

Figure 7: Schematics of the two-terminal device modeled with Eq. (3).

The mean free path will depend on U, but also on the energy, and we need to chose a wide enough device ($l_e << w$) so the system behaves more like a two-dimensional system. In addition, we found that upon varying the value of U, the mean free path varied much strongly than the spin diffusion length (see section below). This fixed our device lengths L on the order of the spin relaxation, and we had to tune U to achieve mean free paths much shorter than L. In this way, we can achieve diffusive transport for both charge ($l_e << L$) and spin. To that end, we use $U = 2$ eV and $w = 50$ nm.

In Fig. 8, we plot the length dependence of the two-terminal conductance and conductivity for two representative energies: $E = 0$ and $E = -105$ meV. As seen from the conductivity

plateaus and shaded regions, only the lengths between 25 and 55 nm are diffusive for the case $E = 0$, and between 45 and 90 nm for $E = -105$ meV. For all energies studied (see Table 3 and insets in Figs. 2 and 3 in the main text), the lengths at which the transport is diffusive varied slightly, but in general ranged from a few tens of nanometers to around 100 nm. In Table 3, we report the mean free paths for all energies studied, as well as the number of modes M, the conductivity σ and the charge diffusion coefficient D_c. The conductivity is extracted by fitting with the formula $G_{2T} = \frac{\sigma w}{x}$, and the diffusion coefficient by $D_c = \frac{1}{2} v_F l_e$, where v_F is the averaged Fermi velocity of all modes at that energy extracted from the band structure of the semiinfinite lead.[25,27] For energies $E \leq -95$ meV, there are not many modes M and therefore we removed the contact resistance $\frac{h}{e^2 M}$ from G_{2T} to account properly for the bulk values of σ and l_e.

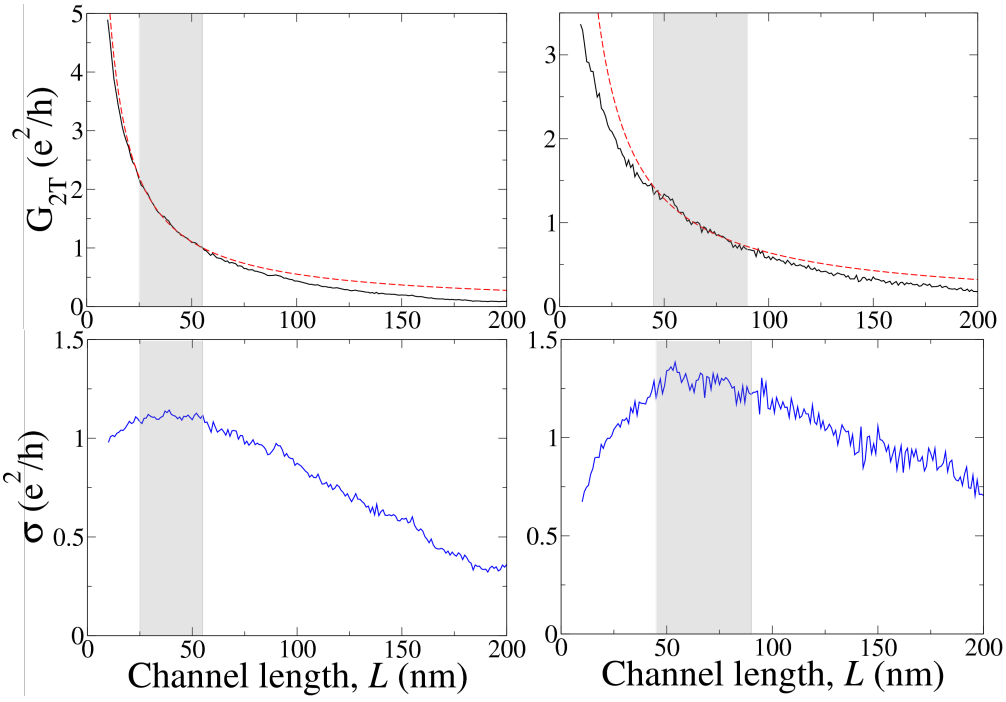

Figure 8: Two-terminal conductance G_{2T} (top) and electrical conductivity σ (bottom) as a function of channel length, L, of $1T_d$-$MoTe_2$ at $E = 0$ (left) and $E = -105$ meV (right). Dashed, red lines are fits with Eq. (8). Shaded, gray regions denote the lengths at which the transport is diffusive, as shown by the conductivity plateaus.

Table 3: Values of the mean free path (l_e), number of modes in the system (M), electrical conductivity (σ) and diffusion coefficient (D_c) for different values of energy E (with respect to the Fermi level). The states at $E = -140$ meV lie in the bulk gap and arise due to the nontrivial band inversion of our model.

E (meV)	l_e (nm)	M	σ (e^2/h)	D_c (cm^2/s)
30	0.88	64	1.12	0.9
0	1.02	54	1.10	1.2
-30	1.55	42	1.30	1.5
-60	1.89	32	1.21	1.6
-80	3.00	22	1.32	2.3
-95	4.50	14	1.25	2.5
-100	6.90	10	1.38	3.4
-105	10.8	6	1.30	4.5
-110	15	4	1.20	4.8
-140	50	2	2	17

Nonlocal spin valve and spin diffusion equation

Here we explain the implementation details of a nonlocal spin valve as well as the equation to fit the length dependence of the nonlocal resistance. To simulate a nonlocal spin valve with Landauer-Büttiker formalism, we need to add two extra semiinfinite leads on top to the two-terminal device described above (see Fig. 9). These two extra leads should model ferromagnetic leads, and to do so we incorporate a spin-dependent hopping between such electrodes and our system $t_\perp = \frac{1}{2}t(\sigma_0 + \kappa\sigma_\alpha)$. Here, t is the interface hopping, σ_0 the identity matrix and $\kappa = [-1, 1]$ is the degree of polarization. Next, to calculate the nonlocal resistance in such a device, we compute the conductance matrix G[28] and solve the linear system of equations $I = GV$, with I and V being vectors describing the current and voltage conditions at each lead. As in experiments, we set up the current to flow between lead 2 to 1, while keeping leads 3 and 4 floating; thus the vector reads $I = (-I_0^\alpha, I_0^\alpha, 0, 0)$, where I_0^α is the injected spin-polarized current. Since the voltage at the lead 1 is grounded, the voltage vector becomes $V = (0, V_2, V_3, V_4)$, with $V_{i=2,3,4}$ being the unknown voltages at leads 2, 3 and 4, respectively. In this manner, the nonlocal resistance becomes $R_{\rm nl}^\alpha = (V_3 - V_4)/I_0^\alpha$. Further

details can be found in a recent publication by some of us.[27]

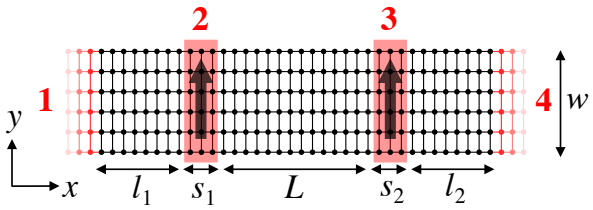

Figure 9: Schematics of the nonlocal spin valve. Black (red) regions denote the device (leads). Leads 2 and 3 are ferromagnetic. Depending on the mean free path and the range of diffusive transport (gray regions in Fig. 8), different values of l_1, L and l_2 were chosen. l_1 ranged between 20 and 50 nm, while $L + l_2$ varied between 70 and 150 nm. w, s_1 and s_2 were kept constant throughout, with values of 50 nm, 1 nm and 1 nm, respectively.

To evaluate the length dependence of $R^{\alpha}_{\rm nl}$, we need to solve the one-dimensional spin diffusion equation:[29–34]

$$\frac{\partial s^{\alpha}}{\partial x} = \frac{1}{\lambda^{\alpha}_{s}} s^{\alpha}, \tag{9}$$

where s^{α} is the spin accumulation or density along the α axis and λ^{α}_{s} is the spin diffusion length for spins pointing along α. One then has $R^{\alpha}_{\rm nl} = \frac{s^{\alpha}}{-2eI^{\alpha}_{0}}$, with $-e$ the electron charge. Typically, this equation is solved by assuming that the spin accumulation has totally relaxed when reaching lead 4 (see Fig. 9). However, if this is not the case, neglecting such spin accumulation at leads 1 and 4 will underestimate the spin diffusion length.[27] To avoid this possibility, we will use a more complete formula that takes into account the effect of leads 1 and 4 in solving Eq. (9):[27]

$$R^{\alpha}_{\rm nl} = \frac{P_i P_d \lambda^{\alpha}_{s}}{2w\sigma} \frac{[\beta \cosh(l_1/\lambda^{\alpha}_{s}) + 4\sinh(l_1/\lambda^{\alpha}_{s})] \cdot [\beta \cosh\left(\frac{L-l}{\lambda^{\alpha}_{s}}\right) - 4\sinh\left(\frac{L-l}{\lambda^{\alpha}_{s}}\right)]}{[4\beta \cosh\left(\frac{l_1+l}{\lambda^{\alpha}_{s}}\right) + (8+\beta^2/2)\sinh\left(\frac{l_1+l}{\lambda^{\alpha}_{s}}\right)]}. \tag{10}$$

Here, $l = L + l_2$ and $\beta = \frac{w\sigma R_c}{\lambda^{\alpha}_{s}}$, with R_c being the contact resistance between lead 1 and the system and between lead 4 and the system (they are assumed the same).

Spin Hall effect and spin accumulation

In this section we derive an expression connecting the spin accumulation at the edges ($x = 0$ and $x = w$) of the device described in Fig. 10a, with the spin Hall angle; and then adapt it to fit the spin accumulation obtained in Kwant.[25] We note that in this case, we drive current along the y direction, in contrast to the previous calculations. This is because we want the spin transport to be along x, so the obtained spin diffusion lengths from the nonlocal spin valve can be taken into account. To start, let us cast the constitutive relations for the charge $\boldsymbol{J}_c$ and spin $\boldsymbol{J}_s^\alpha$ current densities

$$\begin{aligned} \boldsymbol{J}_c &= (\overline{\sigma} - \overline{\sigma}_{\mathrm{sH}}^{\alpha})\boldsymbol{E} - e\overline{D}_c \boldsymbol{\nabla} n_c \\ \boldsymbol{J}_s^\alpha &= \overline{\sigma}_{\mathrm{sH}}^{\alpha}\boldsymbol{E} - e\overline{D}_s^{\alpha} \boldsymbol{\nabla} s^\alpha, \end{aligned} \tag{11}$$

where $\boldsymbol{E}$ the electric field, $\overline{\sigma}$ the electrical conductivity tensor which due to time-reversal symmetry is diagonal

$$\overline{\sigma}_{ij} = \delta_{ij}\sigma_{ii}, \tag{12}$$

n_c the charge density in units of inverse of area, $\overline{D}_c$ the charge diffusion tensor which is proportional to the conductivity by the Einstein's relations, $\overline{D}_s^{\alpha}$ the spin diffusion tensor which we assume to be the same as the charge $\overline{D}_c$ because we consider diffusive transport (thus we drop the superscript α), and $\overline{\sigma}_{\mathrm{sH}}^{\alpha}$ the spin Hall conductivity tensor

$$\overline{\sigma}_{\mathrm{sH}}^{\alpha} = \begin{pmatrix} 0 & \sigma_{xy}^{\alpha} \\ \sigma_{yx}^{\alpha} & 0 \end{pmatrix} \tag{13}$$

where the matrix element σ_{ij}^{α} represents the formation of a spin current flowing along the $i = x, y$ direction with spins polarized in $\alpha = x, y, z$ due to a charge current flowing along $j = x, y$. The difference in the sign of the spin Hall conductivity in the charge and spin

equations (Eq. 11) is a consequence of Onsager's relations, while the absence of diagonal elements in the spin conductivity originates from time-reversal symmetry.

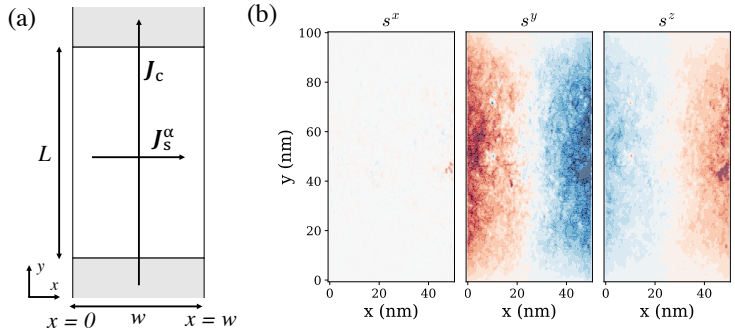

Figure 10: (a) Schematics of the device geometry. Grey (white) regions depict the semiinfinite leads (scattering region). (b) Calculated spin accumulation $s^{\alpha=x,y,z}$ in a device with width 50 nm and length 100 nm. Red (blue) color denotes positive (negative) values of the spin accumulation.

In our device configuration, charge current is mostly driven by the electric field $J_{c,y} \approx \sigma_{yy} E_y$, and although there is an additional contribution coming from the inverse spin Hall effect, it is a second order effect which we will neglect. Since there is only charge current along the y direction, we will drop the y index henceforth. Likewise, the absence of diagonal terms in the spin Hall conductivity imposes that $\boldsymbol{J}_c$ and $\boldsymbol{J}_s^\alpha$ are perpendicular to each other. This allows us to focus only in a single element of the spin diffusion tensor $(\overline{D}_s)_{xx} \rightarrow D_s$ and the spin Hall conductivity $\overline{\sigma}_{\mathrm{sH}}^\alpha \rightarrow \sigma_{xy}^\alpha$. The spin density or accumulation, s^α, can be computed by combining Eq. (11) with the continuity equation

$$\boldsymbol{\nabla} \cdot \boldsymbol{J}_s^\alpha = -e \frac{s^\alpha}{\tau_s^\alpha}, \tag{14}$$

leading to the following diffusion equation

$$\nabla^2 s^\alpha = \frac{s^\alpha}{{\lambda_s^\alpha}^2}, \tag{15}$$

where we have introduced a spin relaxation time τ_s^α for describing the spin relaxation processes, which is related to the spin diffusion length by ${\lambda_s^\alpha}^2 \equiv D_s \tau_s^\alpha$. In our case, the spin density varies only along the x direction, therefore, a general solution for the diffusion equation is

$$s^\alpha(x) = A\mathrm{e}^{-x/\lambda_s^\alpha} + B\mathrm{e}^{x/\lambda_s^\alpha}, \tag{16}$$

which stills needs to be supplemented by the boundary conditions

$$\boldsymbol{J}_s^\alpha(x=0) = 0, \quad \boldsymbol{J}_s^\alpha(x=w) = 0, \tag{17}$$

which by Eq. (11) implies

$$eD_s \frac{ds^\alpha}{dx}\bigg|_{0,w} = \theta_{xy}^\alpha J_c \tag{18}$$

at the edges, where we have introduced the spin Hall angle (SHA) $\theta_{xy}^\alpha \equiv \sigma_{xy}^\alpha/\sigma_{yy}$. Using these boundary conditions one finally finds the spin density

$$s^\alpha(x) = -\frac{\theta_{xy}^\alpha \lambda_s^\alpha J_c}{eD_s} \frac{\sinh\left(\frac{w-2x}{2\lambda_s^\alpha}\right)}{\cosh\left(\frac{w}{2\lambda_s^\alpha}\right)}. \tag{19}$$

This spin density has units of m^{-2} since J_c has units of A/m, λ_s^α has units of m, D_s has units of m^2/s, e has units of Coulomb and θ_{xy}^α is unitless. However, Kwant calculates the spin accumulation response function locally at site i per unit bias voltage V_b at energy E:[25]

$$s_{\mathrm{K},i}^\alpha(E) = \frac{\delta s_i^\alpha(E)}{\delta V_b} = \sum_j^M \psi_i^{j\dagger}(E)\sigma_\alpha \psi_i^j(E), \tag{20}$$

thus having units of V^{-1}. Here, $\psi_i^j(E)$ is the wave function at energy E at site i, originating from the incoming wave function of mode j of one of the leads; σ_α is the Pauli matrix and M is the total number of modes at energy E. We note that in Eq. (19), $\theta_{xy}^\alpha, \lambda_s^\alpha$ and D_s are

also energy-dependent, but we drop the E dependence to keep the equations more compact.

In Fig. 10b, we show $s^{\alpha}_{\mathrm{K},i}(E = 0)$. We chose $w = 50$ nm and $L = 100$ nm so the transport was diffusive for the most part for all energies studied. It is clearly seen that a spin accumulation arises for spins in the y and z direction, but not in x. As commented in the main text, the appearance of an unconventional in-plane component of the spin Hall effect (s^y) is rooted in the low symmetry of the layer group of 1T′ and $1\mathrm{T_d}$ TMDs.[5] Since Eq. (19) describes the spin accumulation along the x direction only, we now need to average the y component of $s^{\alpha}_{\mathrm{K},i}(E)$:

$$s^{\alpha}_{\mathrm{K}}(x) = \frac{\sum_i^N s^{\alpha}_{\mathrm{K,i}}(x, y_i)}{N}, \tag{21}$$

where we have also dropped the E dependence for simplicity. Here, N is the number of sites i along the y direction.

We can finally equate Eq. (19), embodying the spin transport parameters we are interested in, with the averaged simulation output, $s^{\alpha}_{\mathrm{K}}(x)$. If A is the area of site i (corresponding to the area of the rectangular unit cell in our case), we have:

$$s^{\alpha}(x)A = s^{\alpha}_{\mathrm{K}}(x)\frac{V_b}{2\pi}, \tag{22}$$

with the factor 2π appearing naturally in the Landauer-Büttiker formalism.[28,35] We can relate the bias voltage to the current in the linear response regime by $I_c = \frac{e^2}{h}\overline{T}V_b$, where $\overline{T} = MT$ is the two-terminal transmission function (with T the transmission probability per mode) obtained from the two-terminal conductance of the device in Fig. 10a ($G_{2T} = \frac{e^2}{h}\overline{T}$). Together with $I_c = wJ_c$, we obtain:

$$s^{\alpha}(x)A = s^{\alpha}_{\mathrm{K}}(x)\frac{J_c\hbar w}{e^2\overline{T}}. \tag{23}$$

By rearranging the terms and using Eq. (19), we finally arrive at:

$$\frac{s^{\alpha}(x)}{J_c} = s_{\mathrm{K}}^{\alpha}(x)\frac{\hbar w}{e^2 A\overline{T}} = -\frac{\theta_{xy}^{\alpha}\lambda_s^{\alpha}}{eD_s}\frac{\sinh\left(\frac{w-2x}{2\lambda_s^{\alpha}}\right)}{\cosh\left(\frac{w}{2\lambda_s^{\alpha}}\right)}, \tag{24}$$

or alternatively:

$$s_{\mathrm{K}}^{\alpha}(x) = -\theta_{xy}^{\alpha}\lambda_s^{\alpha}\frac{eA\overline{T}}{D_s\hbar w}\frac{\sinh\left(\frac{w-2x}{2\lambda_s^{\alpha}}\right)}{\cosh\left(\frac{w}{2\lambda_s^{\alpha}}\right)}, \tag{25}$$

Hence, we find that we need to add the prefactor $\frac{\hbar w}{e^2 A\overline{T}}$ ($\hbar$ in units J·s) to the output of Kwant to fit it to the solution of the spin drift-diffusion equations. To fit the spin Hall angle, we also need the values of the spin diffusion coefficient and the spin diffusion lengths. The former is taken as the value of D_c obtained from the two-terminal conductance (see values in Table 3), as we consider diffusive transport, and the latter is taken from the nonlocal spin valve simulations by fitting the nonlocal resistance to Eq. (10).

Kubo-Bastin calculations

In order to confirm the validity of our Landauer-Büttiker simulations, we also carry out Kubo-Bastin calculations to obtain the bulk charge and spin Hall conductivities[36] and thus the SHA.

The spin Hall conductivity tensor was computed in the linear response regime by using the Kubo-Bastin formula[37]

$$\sigma_{ij}^{\alpha} = -2\hbar\Omega\int_{-\infty}^{E_{\mathrm{F}}} dE\,\mathrm{Im}\left(\mathrm{Tr}\left[\delta(E-H)J_{s,i}^{\alpha}\frac{dG^{+}}{dE}J_j\right]\right), \tag{26}$$

where Ω is the volume of the sample, J_j the j-th component of the current density operator

which is defined in a localized tight-binding basis by the following expression[38]

$$J_j = \frac{ie}{\Omega\hbar}[H, R_j], \tag{27}$$

with R_j the jth-component of the position operator. The operator $J^{\alpha}_{s,i}$ is the spin current density operator which is defined in terms of the current density as $J^{\alpha}_{s,i} \equiv \{J_i, \sigma_\alpha\}/2$, with σ_α the α Pauli matrix. The spectral operators $\delta(E-H)$ and $G^+ \equiv \lim_{\eta\to 0} 1/(E-H+i\eta)$ are Dirac's delta and retarded Green's function, respectively.

The Green's and Dirac's delta functions in the Kubo-Bastin formula are approximated numerically by using the Kernel Polynomial Method[36,38,39] using 1000 Chebyshev expansion moments, which is equivalent to a broadening of 10 meV for this particular system. The calculations were performed on a system containing $4 \times 1000 \times 1000$ orbitals.

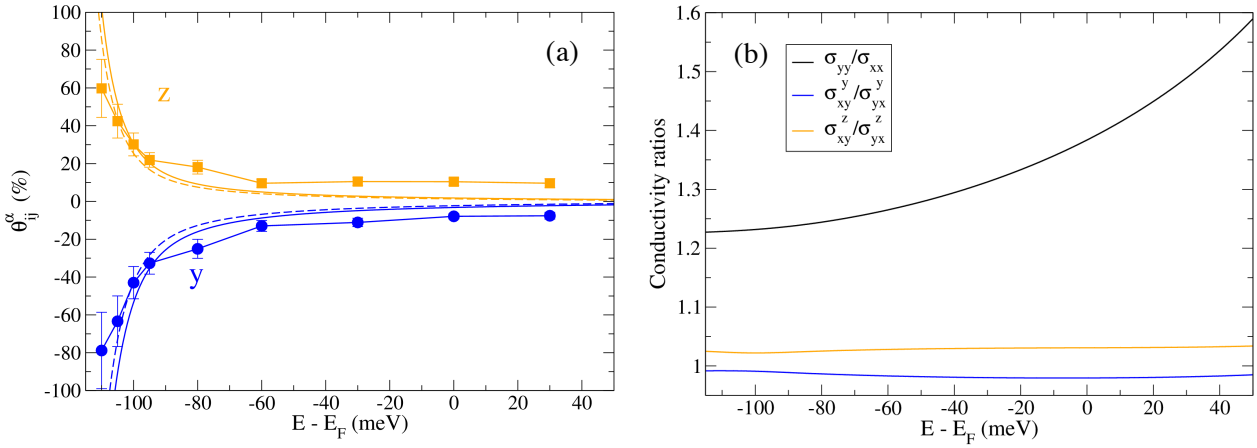

Figure 11: (a) Spin Hall angles as a function of energy for spins in y and in z. Solid lines with circles and squares correspond to Landauer-Büttiker calculations as in the main text ($\theta^{y,z}_{xy}$). Solid (dashed) lines correspond to Kubo-Bastin calculations for $\theta^{y,z}_{xy}$ ($\theta^{y,z}_{yx}$). The positive convention for the SHA is taken when the spin current flows to the right with respect to the charge current (see Fig. 10a). (b) Ratio of charge (black) and spin Hall conductivities (orange and blue).

Here, we compute the spin Hall angle defined as $\theta^{\alpha}_{ij} \equiv \sigma^{\alpha}_{ij}/\sigma_{jj}$ and compare it to the values obtained with the Landauer-Büttiker calculations. We plot the values of the SHA

as a function of the energy in Fig. 11a where a good agreement is clearly seen between both quantum transport methodologies, supporting the validity of our results. Moreover, in Fig. 11b we plot the ratios between the charge and spin Hall conductivities. On the one hand, there is a slight charge transport anisotropy, with the charge conductivity along y being a factor 1.2-1.6 of that of the charge conductivity along x in the energy range studied. On the other hand, the spin Hall conductivity shows an almost isotropic behavior for both spin components. These results imply that the SHA is also slightly anisotropic, with the same factor of the ratio σ_{yy}/σ_{xx}, but nevertheless $|\theta_{xy}^{y,z}|$ and $|\theta_{yx}^{y,z}|$ have the same order of magnitude.

The residual difference between the two methods seen in Fig. 11a is expected due to the averaging over disorder realizations that is performed in LB calculations, in addition to a smaller system size required in the LB case with respect to Kubo-Bastin because of a higher computational cost. The LB calculations were performed for disordered systems with 22750 unit cells, while the Kubo-Bastin calculation of the SHC was performed on a clean system with 10^6 unit cells.

Spin diffusion lengths and persistent spin texture

In general, the relaxation of spins is related to the spin texture of the eigenstates.[33] In our case, the spin texture of conducting electrons (see Figs. 2 and 3 and Fig. 1b in the main text) present two key characteristics:

- The spins mainly lie on the yz plane because the projection along x is negligible, with magnitudes obeying $\langle s^y \rangle_E > \langle s^z \rangle_E \gg \langle s^x \rangle_E$. That is, to a very good approximation, the spins are canted along one direction in the yz plane. Moreover, the y and z projections have opposite sign and the projection along x diminishes as E moves towards the bottom of the conduction band.

- The spin orientation is mostly unchanged throughout the whole Fermi contour. In other words, when "traveling" along the Fermi contour, one sees an approximately persistent spin texture (PST)[40–42] with the above-stated canting of the spins. The PST is not perfect because of the small but finite $\langle s^x \rangle_E$.

The first characteristic is an intrinsic quality of this system appearing due to the form of the spin-orbit coupling in the Hamiltonian, which in turn is dictated by the symmetries of the crystal (as explained in the derivation of the model in the first section of this supplemental material). The relative direction between the y and z components of the spin texture is related to the relative values of the SOC parameters Λ_y and Λ_z.

Most importantly, the second characteristic is crucial to understand the hierarchy we observe for the spin relaxation lengths in the diffusive regime. It is convenient to reason in terms of the natural spin quantization axis in this system, which is precisely that defined by the canting direction of the PST. The (approximate) PST here implies an (approximate) conservation of spin along the canting direction: if we describe the spin orientation with reference to a rotated coordinate system where the z' axis points along the canting direction, the Hamiltonian is (approximately) diagonal with a SOC term proportional to the spin Pauli matrix in that direction, $\sigma_{z'}$. Consequently, when spins are injected collinear to that direction, they enter the system as spin eigenstates. Moreover, the disorder potential, being diagonal in the spin and orbital indices, does not change that - neither at the moment of injection nor during the spin transport in the material -, with the implication that those spins retain a large lifetime (in fact, if the PST were strictly exact, there would be no spin relaxation at all for collinear injection). Conversely, maximum (faster) relaxation is expected for spins injected perpendicularly to z'. The case of spins injected parallel to x is one such case, for which we obtain only numerical noise in the nonlocal spin signal. Therefore, we can correlate the trend in relaxation rate observed in the simulations with the injected spins' projection along z'. Accordingly, the hierarchy $\lambda_s^y > \lambda_s^z$ is a natural reflection of that trend:

spins injected along y have a slightly larger spin diffusion length than those spins injected along z because the y direction lies ~ 30 degrees away from z' compared with ~ 60 degrees for the z direction. Furthermore, because the x component of the spin texture decreases monotonically towards the band edge, the canting direction becomes more aligned with the yz plane, resulting in the increase of both λ_s^y and λ_s^z when E approaches the bottom of the conduction band.

Spin diffusion length of topological edge states

In the main text, the spin diffusion lengths have been evaluated for energies in the conduction band, and the values increase with decreasing energy towards the conduction band minimum. Once the energy lies in the gap and the transport is mediated by the topological edge states (see Fig. 12), the spin diffusion length is expected to diverge as these states are topologically protected against non-magnetic disorder and they propagate ballistically without scattering. Thus, we perform nonlocal transport calculations at energies in the gap (shown as dashed lines in Fig. 12), namely $E = -140$ meV and $E = -320$ meV. The former corresponds to an energy in the gap but relatively close to the conduction band, whereas the latter lies deep in the gap.

Fig. 13 shows the length dependence of $R_{\rm nl}^{\alpha}$ for spins injected with polarization along x, y and z directions. For $E = -140$ meV (Fig. 13a), the behaviour is similar to that of energies in the conduction band; the disorder is strong enough to perturb these edge states lying close to the bulk bands and inducing spin relaxation. Nevertheless, we find spin diffusion lengths much larger than those reported for the conduction band: $\lambda_s^y = 156$ nm and $\lambda_s^z = 56$ nm. On the other hand, for $E = -320$ meV, the nonlocal resistance presents a length-independent value, which is characteristic of ballistic spin transport without spin relaxation.[27]

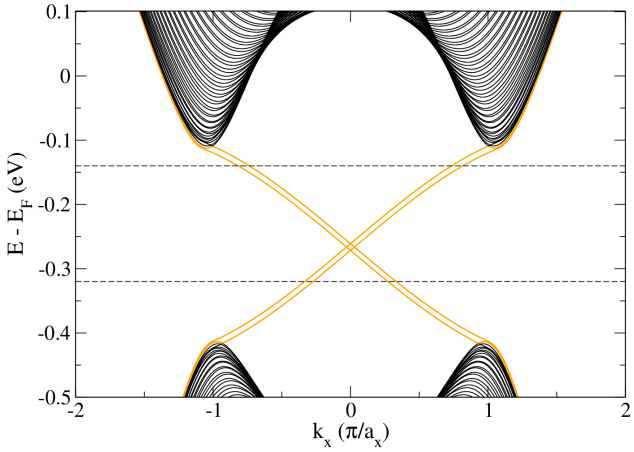

Figure 12: Band structure of a $1T_d$-$MoTe_2$ ribbon with finite width $w = 50$ nm in the y direction. Orange bands depict the topological edge states. Horizontal dashed lines mark the energies $E = -140$ meV and $E = -320$ meV.

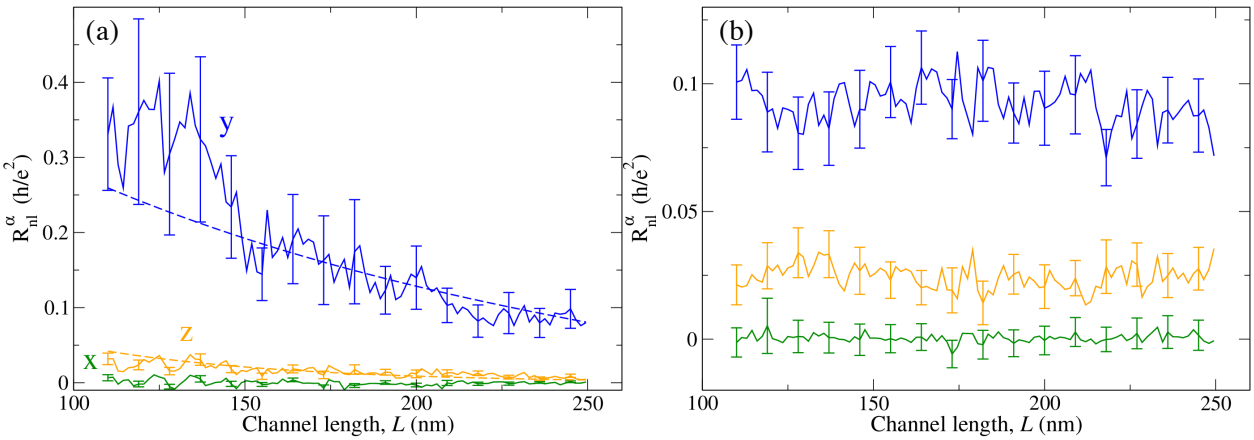

Figure 13: $R^{\alpha}_{\rm nl}$ (solid line) as a function of channel length, L, for spins injected along x, y and z for (a) $E = -140$ meV and (b) $E = -320$ meV. Error bars result from the averaging of 50 disorder configurations. Dashed lines in (a) are fits to Eq. (10). The device lengths are $l_1 = 100$ nm, $L + l_2 = 350$ nm whereas s_1, s_2, w and the Anderson disorder is kept the same as in the calculations presented in the main text.

$1T'$ and $1T_d$ phases of $MoTe_2$

In this section, we compute the nonlocal resistance and spin accumulations for $1T'$-$MoTe_2$. This is obtained by using the same model (Eq. (3)) but setting $\eta = 0$. In this way, inversion symmetry is now preserved, as it is in the $1T'$ phase. All the other parameters, both from the model and from the device geometry, are kept the same.

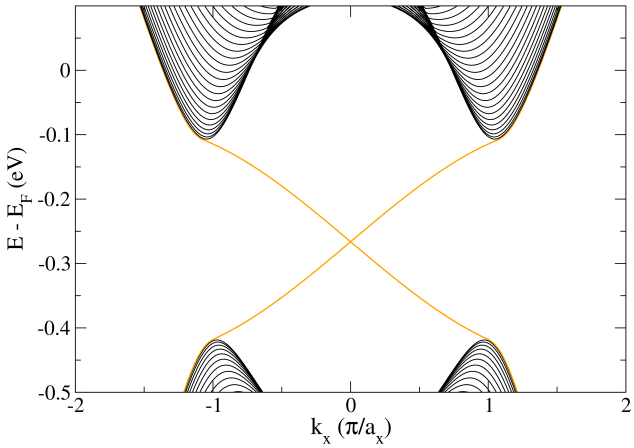

Figure 14: Band structure of a $1T' - MoTe_2$ ribbon with finite width $w = 50$ nm in the y direction. Orange bands depict the topological edge states.

We plot the band structure of a 50-nm-width ribbon in Fig. 14. Clearly, now the spin splitting is absent, as the inversion symmetry is preserved. Except from that, all the other features of the band structure are similar to those of $1T_d$-$MoTe_2$. Next, we show in Fig. 15 the length dependence of the nonlocal resistance calculated in a nonlocal spin valve, and compare it to the corresponding simulation performed in the $1T_d$ phase. We focus on two energies, one at the Fermi level $E = 0$ (Fig. 15a) and the other near the band edge at $E = -105$ meV (Fig. 15b). The two phases present the same scaling of the nonlocal resistance for both y and z polarization of injected spins. Finally, in Fig. 16 we compare the spin accumulations arising due to the spin Hall effect between the two phases at these two energies. The results indicate that the creation of spins along the sample width in $1T'$-$MoTe_2$ is similar to that in $1T_d$-$MoTe_2$.

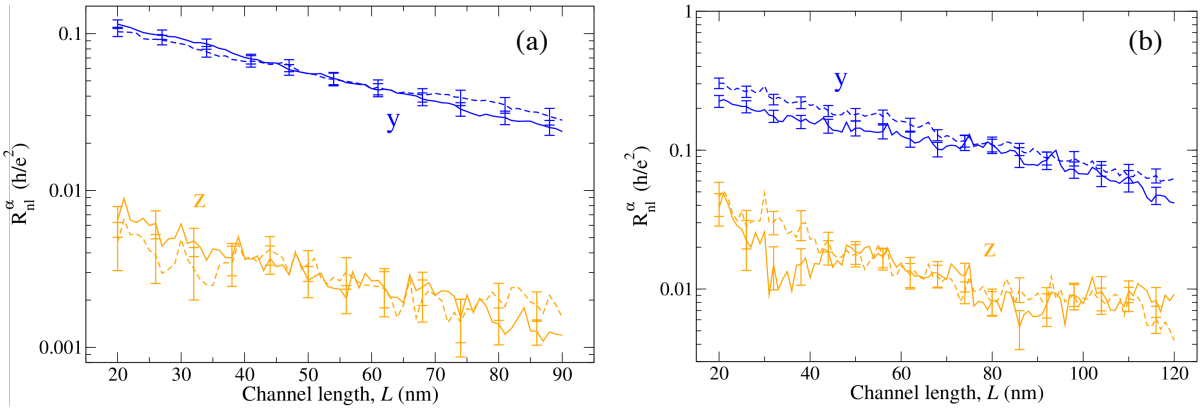

Figure 15: $R_{\rm nl}^{\alpha}$ as a function of channel length, L, for spins injected along y and z for (a) $E = 0$ and (b) $E = 105$ meV. Solid (dashed) lines correspond to a simulation of the T_d (T') phase. Error bars result from the averaging of 150 disorder configurations.

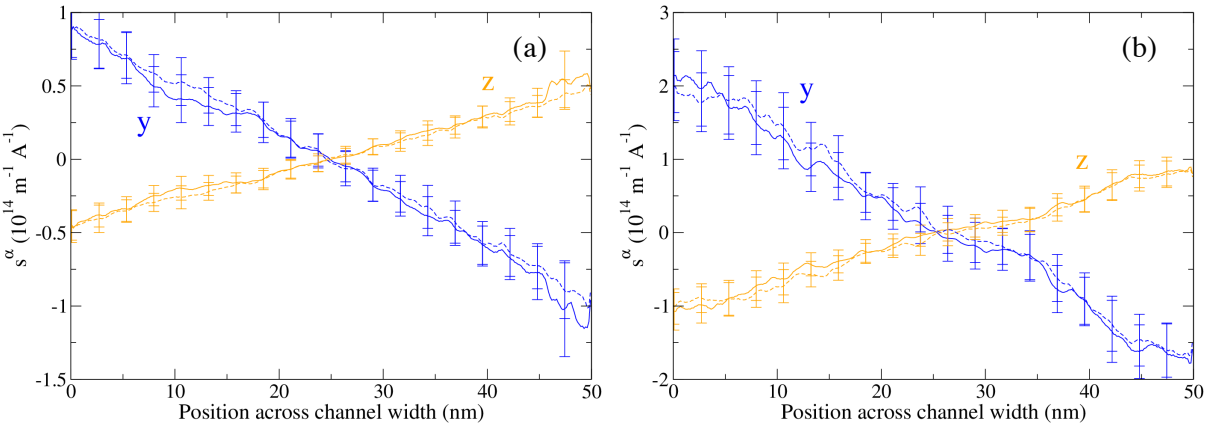

Figure 16: Spin accumulation as a function of position across the channel width of spins along y and z for (a) $E = 0$ and (b) $E = 105$ meV. Solid (dashed) lines correspond to a simulation of the T_d (T') phase. Error bars result from the averaging of 200 and 100 disorder configurations for (a) and (b), respectively.

Experimental setup for measuring the canted spin Hall effect

In this section, we present the formulation to calculate the output voltage in a realistic non-local device, allowing in this way the measurement of the canted SHE. The one-dimensional steady-state Bloch diffusion equation is used to calculate the spin density $\boldsymbol{s} = (s^x, s^y, s^z)$ over the graphene channel and reaching the TMD,[43,44] according to the experimental setup described in the main text. In the presence of an external magnetic field $\boldsymbol{B}$, the diffusion equation reads:

$$D_s \frac{d^2 \boldsymbol{s}}{dx^2} + \gamma_c \, \boldsymbol{s} \times \boldsymbol{B} - \overline{\tau_s^{-1}} \cdot \boldsymbol{s} = 0. \tag{28}$$

The three components of $\boldsymbol{s}$ describe the spin density projected along the corresponding Cartesian axes. $\gamma_c = 2\,\mu_B/\hbar$ is the electron gyromagnetic ratio with μ_B the Bohr magneton and $\overline{\tau_s^{-1}}$ is a 3×3 diagonal matrix containing the spin relaxation times in x, y and z.

Within this model, the spin transport in the device (schematic in Fig. 4, main text) is characterized by simultaneous diffusive and precessional motion under a magnetic field that is chosen to be either along the x or z direction. All the components of $\boldsymbol{s}$ are calculated at any position and, therefore, the spin-current densities that generate the SHE. The solution of Eq. (28) is adapted from Ref.[43] When the TMD crystal is oriented in the configuration shown in Fig 4a of the main text (configuration a), the spin current density with spins in the yz plane, $J_s^{y,z}$, generates a transverse charge current density, J_c, that is detected as a $R_{\mathrm{ISHE}} = V_{\mathrm{ISHE}}/I_0^y$ due to the inverse SHE. Here, I_0^y is the injected current, which is polarized along the direction of the ferromagnetic injector (y in this case, see insets in Fig. 4 in the main text). If the TMD crystal is oriented in the configuration shown in Fig. 4b of the main text (configuration b), J_c is generated by the spin current density with spins along z and x directions (y in the TMD's system of coordinates, which have been rotated with respect to

those in Fig. 4a). In general, J_s^α is,[43]

$$J_s^\alpha = |\boldsymbol{J}_s^\alpha| = \frac{1}{e\, l_{\rm w}\, R_\square} \int_{x_0}^{x_0+l_{\rm w}} \frac{d\, s^\alpha(x)}{dx} dx = \frac{\Delta s^\alpha}{e\, l_{\rm w}\, R_\square}, \tag{29}$$

where $s^\alpha(x)$ is given by Eq. (28) and $\Delta s^\alpha = s^\alpha(x_0 + l_{\rm w}) - s^\alpha(x_0)$. x_0, l_w, $R_\square$ are the distance of the TMD to the injector, the TMD width and its square resistance, respectively. In the simulations presented in Fig. 4 of the main text, we use $x_0 = 3.9\,\mu$m, $l_w = 1.6\,\mu$m and $R_\square = 3.3$ kΩ, and a spin polarization of the FM injector of 10%. Once the spin current of each spin component is known, the generated charge current can be easily obtained given that $J_c = \theta_{xy}^\alpha\, J_s^\alpha$ and $R_{\rm SHE} = J_c\, l_{\rm w}\, R_a / I_0^y$. We note that here the relation between the charge and spin current densities is opposite to that of Eq. (18) since we are dealing with the inverse SHE, which is reciprocal to the SHE. In this way,

$$R_{\rm SHE} = \theta_{xy}^\alpha\, c\, \Delta s^\alpha;\ \text{with}\, c = \frac{R_a}{e R_\square I_0^y}, \tag{30}$$

with R_a the resistance of the TMD channel. The conversion efficiency is related to the spin Hall angle, θ_{xy}^α , which depends on the spin orientation, α. The total charge current density is calculated from the independent contributions of $J_s^{z,y}$.

In the configuration (a) with B_z, $R_{\rm SHE} = -\theta_{xy}^y\, c\, \Delta s^y$, $\theta_{xy}^y = 0.8$. In an experiment the sign depends on the voltage polarity. Here we choose that $R_{\rm SHE} = |\theta_{xy}^y|\, c\, \Delta s^y$, which switches the sign for θ_{xy}^z. For B_x, $R_{\rm SHE} = |\theta_{xy}^y|\, c\, \Delta s^y - |\theta_{xy}^z|\, c\, \Delta s^z$, with $\theta_{xy}^z = 0.5$ and according to the chosen polarity convention. For the configuration (b) with B_z, $R_{\rm SHE} = |\theta_{xy}^y|\, c\, \Delta s^y$, and with B_y, $R_{\rm SHE} = -|\theta_{xy}^z|\, c\, \Delta s^z$. Note that here we are referring according to the TMD system of coordinates (see Fig 4 (b) in the main text).

Finally, we present arguments that show that the spin current flowing in the graphene channel will be absorbed by the TMD. The spin resistance of a material is defined as $R_s =$

$\rho\lambda_s/A$, ρ is the resistivity, λ_s is the spin relaxation length and A the cross area in which the spins flow. An alternative to this definition in terms of the square resistance, is $R_s = R_\square\lambda_s/w_N$, where w_N is the width of the non-magnetic material. In the device proposed, the cross width where spins propagate is the same for graphene (g) and TMD. The ratio of the graphene's spin resistance and the TMD's spin resistance reads as,

$$\frac{R_s^{\mathrm{TMD}}}{R_s^{\mathrm{g}}} = \frac{R_\square^{\mathrm{TMD}}}{R_\square^{\mathrm{g}}}\frac{\lambda_s^{\mathrm{TMD}}}{\lambda_s^{\mathrm{g}}} \tag{31}$$

Using reported values of $R_\square^{\mathrm{g}} \approx 2$ kΩ[44] and $R_\square^{\mathrm{TMD}} \approx 3.3$ kΩ for 1T' $MoTe_2$[45]

$$\frac{R_s^{\mathrm{TMD}}}{R_s^{\mathrm{g}}} \sim \frac{\lambda_s^{\mathrm{TMD}}}{\lambda_s^{\mathrm{g}}} \tag{32}$$

Comparing the calculated $\lambda_s^y \approx 30$ nm with the typical $\lambda_s^{\mathrm{g}} \approx 1.6\,\mu$m,[44] we have that $R_s^{\mathrm{TMD}} \sim 0.01 R_s^{\mathrm{g}}$, and of the same order for λ_s^z.

References

(1) Kresse, G.; Hafner, J. *Physical Review B* **1993**, *48*, 13115–13118.

(2) Kresse, G.; Furthmüller, J. *Computational Materials Science* **1996**, *6*, 15–50.

(3) Kresse, G.; Furthmüller, J. *Physical Review B* **1996**, *54*, 11169–11186.

(4) Chang, T.-R. et al. *Nature Communications* **2016**, *7*, 10639.

(5) Song, P.; Hsu, C.-H.; Vignale, G.; Zhao, M.; Liu, J.; Deng, Y.; Fu, W.; Liu, Y.; Zhang, Y.; Lin, H.; Pereira, V. M.; Loh, K. P. *Nature Materials* **2020**, *19*, 292–298.

(6) Xu, S.-Y. et al. *Nature Physics* **2018**, *14*, 900–906.

(7) Mostofi, A. A.; Yates, J. R.; Pizzi, G.; Lee, Y.-S.; Souza, I.; Vanderbilt, D.; Marzari, N. *Computer Physics Communications* **2014**, *185*, 2309–2310.

(8) Qian, X.; Liu, J.; Fu, L.; Li, J. *Science* **2014**, *346*, 1344–1347.

(9) Fu, L.; Kane, C. L. *Phys. Rev. B* **2007**, *76*, 045302.

(10) Safeer, C. K.; Ontoso, N.; Ingla-Aynés, J.; Herling, F.; Pham, V. T.; Kurzmann, A.; Ensslin, K.; Chuvilin, A.; Robredo, I.; Vergniory, M. G.; de Juan, F.; Hueso, L. E.; Calvo, M. R.; Casanova, F. *Nano Letters* **2019**, *19*, 8758–8766.

(11) Sun, Y.; Wu, S.-C.; Ali, M. N.; Felser, C.; Yan, B. *Phys. Rev. B* **2015**, *92*, 161107.

(12) Wang, Z.; Gresch, D.; Soluyanov, A. A.; Xie, W.; Kushwaha, S.; Dai, X.; Troyer, M.; Cava, R. J.; Bernevig, B. A. *Phys. Rev. Lett.* **2016**, *117*, 056805.

(13) Kim, H.-J.; Kang, S.-H.; Hamada, I.; Son, Y.-W. *Phys. Rev. B* **2017**, *95*, 180101.

(14) Keum, D. H.; Cho, S.; Kim, J. H.; Choe, D.-H.; Sung, H.-J.; Kan, M.; Kang, H.; Hwang, J.-Y.; Kim, S. W.; Yang, H.; Chang, K. J.; Lee, Y. H. *Nature Physics* **2015**, *11*, 482–486.

(15) Tamai, A.; Wu, Q. S.; Cucchi, I.; Bruno, F. Y.; Riccò, S.; Kim, T. K.; Hoesch, M.; Barreteau, C.; Giannini, E.; Besnard, C.; Soluyanov, A. A.; Baumberger, F. *Phys. Rev. X* **2016**, *6*, 031021.

(16) Tang, S.; Zhang, C.; Jia, C.; Ryu, H.; Hwang, C.; Hashimoto, M.; Lu, D.; Liu, Z.; Devereaux, T. P.; Shen, Z.-X.; Mo, S.-K. *APL Materials* **2018**, *6*, 026601.

(17) Song, P.; Hsu, C.; Zhao, M.; Zhao, X.; Chang, T.-R.; Teng, J.; Lin, H.; Loh, K. P. *2D Materials* **2018**, *5*, 031010.

(18) Pawlik, A.-S.; Aswartham, S.; Morozov, I.; Knupfer, M.; Büchner, B.; Efremov, D. V.; Koitzsch, A. *Phys. Rev. Materials* **2018**, *2*, 104004.

(19) Zhao, C.; Hu, M.; Qin, J.; Xia, B.; Liu, C.; Wang, S.; Guan, D.; Li, Y.; Zheng, H.; Liu, J.; Jia, J. *Phys. Rev. Lett.* **2020**, *125*, 046801.

(20) Tang, S. et al. *Nature Physics* **2017**, *13*, 683–687.

(21) Fei, Z.; Palomaki, T.; Wu, S.; Zhao, W.; Cai, X.; Sun, B.; Nguyen, P.; Finney, J.; Xu, X.; Cobden, D. H. *Nature Physics* **2017**, *13*, 677–682.

(22) Jia, Z.-Y.; Song, Y.-H.; Li, X.-B.; Ran, K.; Lu, P.; Zheng, H.-J.; Zhu, X.-Y.; Shi, Z.-Q.; Sun, J.; Wen, J.; Xing, D.; Li, S.-C. *Phys. Rev. B* **2017**, *96*, 041108.

(23) Wu, S.; Fatemi, V.; Gibson, Q. D.; Watanabe, K.; Taniguchi, T.; Cava, R. J.; Jarillo-Herrero, P. *Science* **2018**, *359*, 76–79.

(24) Shi, Y.; Kahn, J.; Niu, B.; Fei, Z.; Sun, B.; Cai, X.; Francisco, B. A.; Wu, D.; Shen, Z.-X.; Xu, X.; Cobden, D. H.; Cui, Y.-T. *Science Advances* **2019**, *5*.

(25) Groth, C. W.; Wimmer, M.; Akhmerov, A. R.; Waintal, X. *New J. Phys.* **2014**, *16*, 063065.

(26) Foa Torres, L. E. F.; Roche, S.; Charlier, J. C. *Introduction to Graphene-Based Nanomaterials: FromElectronic Structure to QuantumTransport*; Cambridge University Press, 2014.

(27) Vila, M.; Garcia, J. H.; Cummings, A. W.; Power, S. R.; Groth, C. W.; Waintal, X.; Roche, S. *Phys. Rev. Lett.* **2020**, *124*, 196602.

(28) Datta, S. *Electronic transport in mesoscopic systems*; Cambridge University Press, 1997.

(29) Johnson, M.; Silsbee, R. H. *Phys. Rev. Lett.* **1985**, *55*, 1790–1793.

(30) Johnson, M.; Silsbee, R. H. *Phys. Rev. B* **1988**, *37*, 5312–5325.

(31) Jedema, F.; Heersche, H.; Filip, A.; Baselmans, J.; Van Wees, B. *Nature* **2002**, *416*, 713–716.

(32) Žutić, I.; Fabian, J.; Das Sarma, S. *Reviews of Modern Physics* **2004**, *76*, 323–410.

(33) Fabian, J.; Matos-Abiaguea, A.; Ertler, P., C. snd Stano; Žutić, I. *Acta Phys. Slovaca* **2007**, *57*, 565–907.

(34) Wu, M.; Jiang, J.; Weng, M. *Physics Reports* **2010**, *493*, 61 – 236.

(35) Gaury, B.; Weston, J.; Santin, M.; Houzet, M.; Groth, C.; Waintal, X. *Physics Reports* **2014**, *534*, 1–37.

(36) García, J. H.; Covaci, L.; Rappoport, T. G. *Phys. Rev. Lett.* **2015**, *114*, 116602.

(37) Bastin, A.; Lewiner, C.; Betbeder-matibet, O.; Nozieres, P. *Journal of Physics and Chemistry of Solids* **1971**, *32*, 1811 – 1824.

(38) Fan, Z.; Garcia, J.; Cummings, A.; Barrios-Vargas, J.; Panhans, M.; Harju, A.; Ortmann, F.; Roche, S. *arXiv:1811.07387* **2019**,

(39) Garcia, J. H.; Vila, M.; Cummings, A. W.; Roche, S. *Chem. Soc. Rev.* **2018**, *47*, 3359–3379.

(40) Schliemann, J.; Egues, J. C.; Loss, D. *Phys. Rev. Lett.* **2003**, *90*, 146801.

(41) Bernevig, B. A.; Orenstein, J.; Zhang, S.-C. *Phys. Rev. Lett.* **2006**, *97*, 236601.

(42) Schliemann, J. *Rev. Mod. Phys.* **2017**, *89*, 11001.

(43) Benítez, L. A.; Savero Torres, W.; Sierra, J. F.; Timmermans, M.; Garcia, J. H.; Roche, S.; Costache, M. V.; Valenzuela, S. O. *Nature Materials* **2020**, *19*, 170–175.

(44) Benítez, L. A.; Sierra, J. F.; Savero Torres, W.; Timmermans, M.; Costache, M. V.; Valenzuela, S. O. *APL Mater.* **2019**, *7*, 120701.

(45) Zhou, L.; Zubair, A.; Wang, Z.; Zhang, X.; Ouyang, F.; Xu, K.; Fang, W.; Ueno, K.; Li, J.; Palacios, T.; Kong, J.; Dresselhaus, M. S. *Adv. Mater.* **2016**, *28*, 9526–9531.